






Discovery of a New Gamma-Ray Source, LHAASO J0341+5258, with Emission up to 200 TeV

Zhen Cao^{1,2,3}, F. Aharonian^{4,5} , Q. An^{6,7}, Axikegu⁸, L. X. Bai⁹, Y. X. Bai^{1,3}, Y. W. Bao¹⁰, D. Bastieri¹¹, X. J. Bi^{1,2,3}, Y. J. Bi^{1,3}, H. Cai¹², J. T. Cai¹¹, Zhe Cao^{6,7}, J. Chang¹³, J. F. Chang^{1,3,6}, B. M. Chen¹⁴, E. S. Chen^{1,2,3}, J. Chen⁹, Liang Chen^{1,2,3}, Liang Chen¹⁵, Long Chen⁸, M. J. Chen^{1,3}, M. L. Chen^{1,3,6}, Q. H. Chen⁸, S. H. Chen^{1,2,3}, S. Z. Chen^{1,3} , T. L. Chen¹⁶, X. L. Chen^{1,2,3}, Y. Chen¹⁰, N. Cheng^{1,3}, Y. D. Cheng^{1,3}, S. W. Cui¹⁴, X. H. Cui¹⁷, Y. D. Cui¹⁸, B. D'Ettoire Piazzoli¹⁹, B. Z. Dai²⁰, H. L. Dai^{1,3,6}, Z. G. Dai⁷, Danzengluobu¹⁶, D. della Volpe²¹, X. J. Dong^{1,3}, K. K. Duan¹³, J. H. Fan¹¹, Y. Z. Fan¹³, Z. X. Fan^{1,3}, J. Fang²⁰, K. Fang^{1,3}, C. F. Feng²², L. Feng¹³, S. H. Feng^{1,3}, Y. L. Feng¹³, B. Gao^{1,3}, C. D. Gao²², L. Q. Gao^{1,2,3}, Q. Gao¹⁶, W. Gao²², M. M. Ge²⁰, L. S. Geng^{1,3}, G. H. Gong²³, Q. B. Gou^{1,3}, M. H. Gu^{1,3,6}, F. L. Guo¹⁵, J. G. Guo^{1,2,3}, X. L. Guo⁸, Y. Q. Guo^{1,3}, Y. Y. Guo^{1,2,3,13}, Y. A. Han²⁴, H. H. He^{1,2,3}, H. N. He¹³, J. C. He^{1,2,3}, S. L. He¹¹, X. B. He¹¹, Y. He⁸, M. Heller²¹, Y. K. Hor¹⁸, C. Hou^{1,3}, H. B. Hu^{1,2,3}, S. Hu⁹, S. C. Hu^{1,2,3}, X. J. Hu²³, D. H. Huang⁸, Q. L. Huang^{1,3}, W. H. Huang²², X. T. Huang²², X. Y. Huang¹³, Z. C. Huang⁸, F. Ji^{1,3}, X. L. Ji^{1,3,6}, H. Y. Jia⁸, K. Jiang^{6,7}, Z. J. Jiang²⁰, C. Jin^{1,2,3}, T. Ke^{1,3}, D. Kuleshov²⁵, K. Levochkin²⁵, B. B. Li¹⁴, Cheng Li^{6,7}, Cong Li^{1,3} , F. Li^{1,3,6}, H. B. Li^{1,3}, H. C. Li^{1,3}, H. Y. Li^{7,13}, J. Li^{1,3,6}, K. Li^{1,3}, W. L. Li²², X. R. Li^{1,3}, Xin Li^{6,7}, Xin Li⁸, Y. Li⁹, Y. Z. Li^{1,2,3}, Zhe Li^{1,3}, Zhuo Li²⁶, E. W. Liang²⁷, Y. F. Liang²⁷, S. J. Lin¹⁸, B. Liu⁷, C. Liu^{1,3}, D. Liu²², H. Liu⁸, H. D. Liu²⁴, J. Liu^{1,3}, J. L. Liu²⁸, J. S. Liu¹⁸, J. Y. Liu^{1,3}, M. Y. Liu¹⁶, R. Y. Liu¹⁰, S. M. Liu⁸, W. Liu^{1,3}, Y. Liu¹¹, Y. N. Liu²³, Z. X. Liu⁹, W. J. Long⁸, R. Lu²⁰, H. K. Lv^{1,3}, B. Q. Ma²⁶, L. L. Ma^{1,3}, X. H. Ma^{1,3}, J. R. Mao²⁹, A. Masood⁸, Z. Min^{1,3}, W. Mitthumsiri³⁰, T. Montaruli²¹, Y. C. Nan²², B. Y. Pang⁸, P. Pattarakijwanich³⁰, Z. Y. Pei¹¹, M. Y. Qi^{1,3}, Y. Q. Qi¹⁴, B. Q. Qiao^{1,3}, J. J. Qin⁷, D. Ruffolo³⁰, V. Rubev²⁵, A. Sáiz³⁰, L. Shao¹⁴, O. Shchegolev^{25,31}, X. D. Sheng^{1,3}, J. Y. Shi^{1,3}, H. C. Song²⁶, Yu. V. Stenkin^{25,31}, V. Stepanov²⁵, Y. Su³², Q. N. Sun⁸, X. N. Sun²⁷, Z. B. Sun³³, P. H. T. Tam¹⁸, Z. B. Tang^{6,7}, W. W. Tian^{2,17}, B. D. Wang^{1,3}, C. Wang³³, H. Wang⁸, H. G. Wang¹¹, J. C. Wang²⁹, J. S. Wang²⁸, L. P. Wang²², L. Y. Wang^{1,3}, R. N. Wang⁸, W. Wang¹⁸, W. Wang¹², X. G. Wang²⁷, X. J. Wang^{1,3}, X. Y. Wang¹⁰, Y. Wang⁸, Y. D. Wang^{1,3}, Y. J. Wang^{1,3}, Y. P. Wang^{1,2,3}, Z. H. Wang⁹, Z. X. Wang²⁰, Zhen Wang²⁸, Zheng Wang^{1,3,6}, D. M. Wei¹³, J. J. Wei¹³, Y. J. Wei^{1,2,3}, T. Wen²⁰, C. Y. Wu^{1,3}, H. R. Wu^{1,3}, S. Wu^{1,3}, W. X. Wu⁸, X. F. Wu¹³, S. Q. Xi^{1,3}, J. Xia^{7,13}, J. J. Xia⁸, G. M. Xiang^{2,15}, D. X. Xiao¹⁶, G. Xiao^{1,3}, H. B. Xiao¹¹, S. G. Xin¹², Y. L. Xin⁸, Y. Xing¹⁵, D. L. Xu²⁸, R. X. Xu²⁶, L. Xue²², D. H. Yan²⁹, J. Z. Yan¹³, C. W. Yang⁹, F. F. Yang^{1,3,6}, J. Y. Yang¹⁸, L. L. Yang¹⁸, M. J. Yang^{1,3}, R. Z. Yang⁷, S. B. Yang²⁰, Y. H. Yao⁹, Z. G. Yao^{1,3}, Y. M. Ye²³, L. Q. Yin^{1,3}, N. Yin²², X. H. You^{1,3}, Z. Y. You^{1,2,3}, Y. H. Yu²², Q. Yuan¹³, H. D. Zeng¹³, T. X. Zeng^{1,3,6}, W. Zeng²⁰, Z. K. Zeng^{1,2,3}, M. Zha^{1,3}, X. X. Zhai^{1,3}, B. B. Zhang¹⁰, H. M. Zhang¹⁰, H. Y. Zhang²², J. L. Zhang¹⁷, J. W. Zhang⁹, L. X. Zhang¹¹, Li Zhang²⁰, Lu Zhang¹⁴, P. F. Zhang²⁰, P. P. Zhang¹⁴, R. Zhang^{7,13}, S. R. Zhang¹⁴, S. S. Zhang^{1,3}, X. Zhang¹⁰, X. P. Zhang^{1,3}, Y. F. Zhang⁸, Y. L. Zhang^{1,3}, Yi Zhang^{1,13}, Yong Zhang^{1,3}, B. Zhao⁸, J. Zhao^{1,3}, L. Zhao^{6,7}, L. Z. Zhao¹⁴, S. P. Zhao^{15,22}, F. Zheng³³, Y. Zheng⁸, B. Zhou^{1,3}, H. Zhou²⁸, J. N. Zhou¹⁵, P. Zhou¹⁰, R. Zhou⁹, X. X. Zhou⁸, C. G. Zhu²², F. R. Zhu⁸, H. Zhu¹⁷, K. J. Zhu^{1,2,3,6}, and X. Zuo^{1,3}

¹ Key Laboratory of Particle Astrophysics & Experimental Physics Division & Computing Center, Institute of High Energy Physics, Chinese Academy of Sciences, 100049 Beijing, People's Republic of China; licong@ihep.ac.cn, chensz@ihep.ac.cn, wusha@ihep.ac.cn

² University of Chinese Academy of Sciences, 100049 Beijing, People's Republic of China

³ TIANFU Cosmic Ray Research Center, Chengdu, Sichuan, People's Republic of China

⁴ Dublin Institute for Advanced Studies, 31 Fitzwilliam Place, 2 Dublin, Ireland

⁵ Max-Planck-Institut für Kernphysik, P.O. Box 103980, D-69029 Heidelberg, Germany

⁶ State Key Laboratory of Particle Detection and Electronics, People's Republic of China

⁷ University of Science and Technology of China, 230026 Hefei, Anhui, People's Republic of China; yangrz@ustc.edu.cn, lbing@ustc.edu.cn

⁸ School of Physical Science and Technology & School of Information Science and Technology, Southwest Jiaotong University, 610031 Chengdu, Sichuan, People's Republic of China

⁹ College of Physics, Sichuan University, 610065 Chengdu, Sichuan, People's Republic of China

¹⁰ School of Astronomy and Space Science, Nanjing University, 210023 Nanjing, Jiangsu, People's Republic of China

¹¹ Center for Astrophysics, Guangzhou University, 510006 Guangzhou, Guangdong, People's Republic of China

¹² School of Physics and Technology, Wuhan University, 430072 Wuhan, Hubei, People's Republic of China

¹³ Key Laboratory of Dark Matter and Space Astronomy, Purple Mountain Observatory, Chinese Academy of Sciences, 210023 Nanjing, Jiangsu, People's Republic of China

¹⁴ Hebei Normal University, 050024 Shijiazhuang, Hebei, People's Republic of China

¹⁵ Key Laboratory for Research in Galaxies and Cosmology, Shanghai Astronomical Observatory, Chinese Academy of Sciences, 200030 Shanghai, People's Republic of China

¹⁶ Key Laboratory of Cosmic Rays (Tibet University), Ministry of Education, 850000 Lhasa, Tibet, People's Republic of China

¹⁷ National Astronomical Observatories, Chinese Academy of Sciences, 100101 Beijing, People's Republic of China

¹⁸ School of Physics and Astronomy & School of Physics (Guangzhou), Sun Yat-sen University, 519000 Zhuhai, Guangdong, People's Republic of China

¹⁹ Dipartimento di Fisica dell'Università di Napoli "Federico II," Complesso Universitario di Monte Sant'Angelo, via Cintia, I-80126 Napoli, Italy

²⁰ School of Physics and Astronomy, Yunnan University, 650091 Kunming, Yunnan, People's Republic of China

²¹ D'épartement de Physique Nucléaire et Corpusculaire, Faculté de Sciences, Université de Genève, 24 Quai Ernest Ansermet, 1211 Geneva, Switzerland

²² Institute of Frontier and Interdisciplinary Science, Shandong University, 266237 Qingdao, Shandong, People's Republic of China

²³ Department of Engineering Physics, Tsinghua University, 100084 Beijing, People's Republic of China

²⁴ School of Physics and Microelectronics, Zhengzhou University, 450001 Zhengzhou, Henan, People's Republic of China

²⁵ Institute for Nuclear Research of Russian Academy of Sciences, 117312 Moscow, Russia

²⁶ School of Physics, Peking University, 100871 Beijing, People's Republic of China

²⁷ School of Physical Science and Technology, Guangxi University, 530004 Nanning, Guangxi, People's Republic of China

²⁸ Tsung-Dao Lee Institute & School of Physics and Astronomy, Shanghai Jiao Tong University, 200240 Shanghai, People's Republic of China

²⁹ Yunnan Observatories, Chinese Academy of Sciences, 650216 Kunming, Yunnan, People's Republic of China

³⁰ Department of Physics, Faculty of Science, Mahidol University, 10400 Bangkok, Thailand

³¹ Moscow Institute of Physics and Technology, 141700 Moscow, Russia

³² Key Laboratory of Radio Astronomy, Purple Mountain Observatory, Chinese Academy of Sciences, 210023 Nanjing, Jiangsu, People's Republic of China

³³ National Space Science Center, Chinese Academy of Sciences, 100190 Beijing, People's Republic of China

Received 2021 May 31; revised 2021 June 27; accepted 2021 June 30; published 2021 August 11

Abstract

We report the discovery of a new unidentified extended γ -ray source in the Galactic plane named LHAASO J0341+5258 with a pretrial significance of 8.2 standard deviations above 25 TeV. The best-fit position is R.A. = $55^{\circ}34 \pm 0^{\circ}11$ and decl. = $52^{\circ}97 \pm 0^{\circ}07$. The angular size of LHAASO J0341+5258 is $0^{\circ}29 \pm 0^{\circ}06_{\text{stat}} \pm 0^{\circ}02_{\text{sys}}$. The flux above 25 TeV is about 20% of the flux of the Crab Nebula. Although a power-law fit of the spectrum from 10 to 200 TeV with the photon index $\alpha = 2.98 \pm 0.19_{\text{stat}} \pm 0.02_{\text{sys}}$ is not excluded, the LHAASO data together with the flux upper limit at 10 GeV set by the Fermi-LAT observation, indicate a noticeable steepening of an initially hard power-law spectrum with a cutoff at ≈ 50 TeV. We briefly discuss the origin of ultra-high-energy gamma rays. The lack of an energetic pulsar and a young supernova remnant inside or in the vicinity of LHAASO J0341+5258 challenge, but do not exclude, both the leptonic and hadronic scenarios of gamma-ray production.

Unified Astronomy Thesaurus concepts: Particle astrophysics (96)

1. Introduction

The distinct cosmic-ray spectral feature around 10^{15} eV, the so-called “knee,” in the locally measured cosmic-ray spectrum implies that the galaxy contains objects accelerating protons and nuclei to PeV energies. Identification of these accelerators or the so-called PeVatrons is a prime objective toward the understanding of the origin of galactic cosmic rays. Gamma rays and neutrinos, produced in the interaction of cosmic rays with the ambient medium within or around the accelerator, are key signatures of these cosmic-ray factories.

Over the last two decades, more than 200 very high-energy (VHE, >0.1 TeV) γ -ray sources have been reported³⁴ due to the successful operation of imaging atmospheric Cherenkov telescopes (IACTs) and extensive air shower (EAS) arrays. Although there is much progress made in recent years, the origin of cosmic rays is still an open question. The spectrum of most of the reported gamma-ray sources can be well explained by the inverse Compton scattering of directly accelerated electrons. Further exploration in the TeV–PeV energy band is necessary to pin down which kind of source could explain the cosmic rays up to the knee and beyond.

The proposed possible candidates for galactic PeVatron include supernova remnants (SNRs) (for a review, see, e.g., Aharonian 2013), young massive star clusters (Aharonian et al. 2019), the supermassive black hole in the Galactic Center (HESS Collaboration et al. 2016), pulsars (Bednarek & Protheroe 2002), etc. Observations of the γ -ray sky above tens of TeV, especially in the ultra-high-energy band (UHE, >0.1 PeV), are crucial for searching and identifying PeVatrons. The current generation of IACTs is most sensitive at TeV energies. However, the low flux of photons above 10 TeV requires large exposure, which is limited by the duty cycle and few-degree field of view (FoV) of IACTs. On the other hand, EAS arrays, such as Tibet-As γ and HAWC, have a high duty cycle and wide FoV, so that they can detect gamma-ray sources beyond energies of tens of TeV (Amenomori et al. 2019; Abeysekara et al. 2020).

LHAASO is a large hybrid EAS array being constructed on the Haizi Mountain, Daocheng, Sichuan province, China. It is

composed of three subarrays, including the 1 km² array (KM2A), the water Cherenkov detector array, and the wide-field air Cherenkov/fluorescence telescopes array (He 2018). Being the most sensitive observatory above a few tens of TeV currently in operation, LHAASO can survey the sky in the decl. band from -15° to 75° with full duty cycle and has the potential to find new sources at UHE (Cao et al. 2019). Even though only half of KM2A has been operated since the end of 2019, the sensitivity is already better than what has been achieved by previous observations above tens of TeV. Benefiting from the excellent sensitivity, LHAASO has detected 12 UHE sources with a statistical significance greater than 7σ (Cao et al. 2021). A detailed study of the performance of KM2A via the observation of the Crab Nebula is presented in Aharonian et al. (2021). In this paper, we report on the detection and study of primary properties of a newly discovered source above tens of TeV. Possible counterparts in other wavelengths and different possible production scenarios are discussed.

2. The LHAASO-KM2A Experiment

The whole KM2A array consists of 5195 electromagnetic particle detectors (EDs) and 1188 muon detectors (MDs), which are spread over a 1.3 km² area. The EDs and MDs are used to detect the number of secondary particles and record their arrival time. The ED is a scintillation detector covered by a 5 mm thick lead plate to absorb low-energy charged particles and to convert high-energy γ -rays into electron–positron pairs. The MD is a water Cherenkov detector with ultra-pure water as a detection medium. The detector is covered by overburdened soil with a thickness of 2.5 m, which absorbs most of the secondary electron/positrons and γ -rays. More details about the detectors are presented in He (2018). About half of the detectors have been installed and started operation since the end of 2019.

Once more than 20 EDs are fired within a time window of 400 ns, a shower will trigger the array, and all hits within 5 μ s before and after the trigger time will be recorded. An offline method has been developed to calibrate the time measurements of EDs. The charge measurements of EDs are calibrated by selecting single minimum ionization particle (MIP) events in

³⁴ <http://tevcat.uchicago.edu/>

the EAS. More details about ED calibration can be found elsewhere (Lv et al. 2018). The calibration of time and charge responses for MDs is similar to the calibration for EDs. With the calibration of each detector, the ADC counts of EDs and MDs are converted into the number of particles. The status of each detector is monitored in real time, and only detectors under normal conditions are used for reconstruction.

Both measured and simulated events are processed through the same reconstruction pipeline. The direction of showers is reconstructed by fitting the relative arriving time of the ED hits. The angular resolution (denoted as ϕ_{68} , containing 68% of the events) is $0^\circ.5\text{--}0^\circ.8$ at 20 TeV and $0^\circ.24\text{--}0^\circ.3$ at 100 TeV for γ -ray showers at different zenith angles. The parameter ρ_{50} , defined as the particle density at 50 m from the shower axis obtained by fitting the Nishimura–Kamata–Greisen (NKG) function to the shower hits, is used as an energy estimator (Aharonian et al. 2021). The energy resolution is about 24% at 20 TeV and 13% at 100 TeV for showers with a zenith angle less than 20° . Considering there are more muons and fewer electrons in hadronic showers than in electromagnetic showers of the same energy, the ratio between muons and electrons is used to discriminate electromagnetic showers from hadronic showers. The survival ratio for protons and nucleus is about 1×10^{-3} at 40 TeV, with 48% of gamma rays surviving. The rejection power will be better at higher energies. The data reconstruction, calibration, and selection are described in detail in Aharonian et al. (2021).

3. Analysis and Results

The data used in this analysis were collected from 2019 December to 2020 November by half of KM2A. The total effective observation time is 308.33 days after the data quality check, and then the same event reconstruction and selection are used as described in the performance paper (Aharonian et al. 2021). The dedicated observation time on LHAASO J0341+5258 is 2368.7 hr.

Considering the energy resolution and statistics, one decade of energy is divided into five bins with a bin width of $\log_{10}E = 0.2$. The sky in celestial coordinates (R.A. and decl.) is divided into grids with size of $0^\circ.1 \times 0^\circ.1$ and filled with detected events according to their reconstructed arrival directions for each energy bin. The “direct integration method” (Fleysher et al. 2004) is adopted to estimate the number of cosmic-ray background events. This method uses events with the same direction in horizontal coordinates but at different arrival times to estimate the background. An integration of 24 hr of off-source data is used to estimate the background in this work. There are some local effects, such as the galactic diffuse gamma emission, which may also influence the results. The ratio of the total events to the total background events at a distance between 1.5 and 3.5 from the center of the source is used to remove this effect. The test statistic used to evaluate the significance of the test is $TS = 2\log(\lambda)$, where $\lambda = \mathcal{L}_{s+b}/\mathcal{L}_b$. \mathcal{L}_{s+b} is the maximum likelihood value for the source plus background hypothesis, while \mathcal{L}_b is the background-only hypothesis. According to Wilks’ Theorem (Wilks 1938), TS follows a chi-square distribution with the number of degrees of freedom equal to the difference in the number of free parameters between the hypotheses. In this work, a two-dimensional Gaussian model with sigma fixed at $\phi_{68}/1.51$ is used, and the only free parameter is the total number of events. Thus, we can take $\pm\sqrt{TS}$ as the significance of observed results.

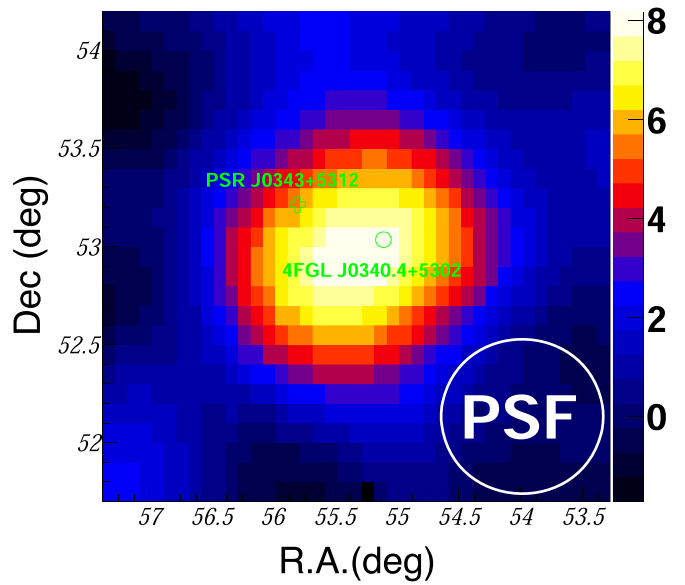


Figure 1. The significance map of LHAASO J0341+5258 above 25 TeV. The green circle marks the position of 4FGL J0340.4+5302, and the blue cross marks the position of the pulsar PSR J0343+5312. The white circle at the bottom-right corner shows the size of the PSF (68% containment). The PSF value is $0^\circ.40$ above 25 TeV.

The significance map for energies above 25 TeV is shown in Figure 1, and the highest pretrial significance value is 8.2σ . Probabilities must be scaled by a trial factor accounting for the number of attempts to find a source, here conservatively assumed to be equal to the number of bins in the sky map (3600×900). The significance after trials is about 6.0σ . It should be noted that the trials are overestimated here; because the smoothing radius is larger than the bin width, the significance in adjacent bins is correlated.

The method to determine the position and extension of the source is similar to the above description. However, the position and extension of the source are left as free parameters. The intrinsic extension is determined to be $\sigma_{\text{ext}} = 0^\circ.29 \pm 0^\circ.06$. The best-fit position is R.A. = $55^\circ.34 \pm 0^\circ.11$ and decl. = $52^\circ.97 \pm 0^\circ.07$. The potential inconsistency between simulation and data on the point-spread function is the main systematic error, which has an impact of $0^\circ.02$ on extension. To study the significance of the extension of the source, we compared the ΔTS between the extensive and point-source assumptions, which results in a ΔTS of 13.3. The extensive source assumption is favored at 3.6σ .

The intrinsic extension of J0341+5258 is checked by comparing the distribution of θ^2 for signals between experiment and simulation as shown in Figure 2, where θ is the angular distance of each event to the position of J0341+5258. A set of γ -rays are generated taking into account the spectral energy distribution (SED), the intrinsic source extension, and the detector PSF. The good agreement between simulation and experimental results with $\chi^2/ndf = 7.4/8$ demonstrates the correct understanding of the extension of the source.

We estimate the spectrum of LHAASO J0341+5258 using a forward-folding method, described in Aharonian et al. (2021). The total number of events in each energy bin is generated by simulating the detector’s response to each event and assuming a power-law spectrum $f(E) = J \cdot (E/E_0)^{-\alpha}$. The reference energy E_0 is chosen to be 40 TeV here. The best-fit values of J and α are obtained by minimizing χ^2 function. The spectral energy distribution ($E^2 dN/dE$) is shown in Figure 3. The

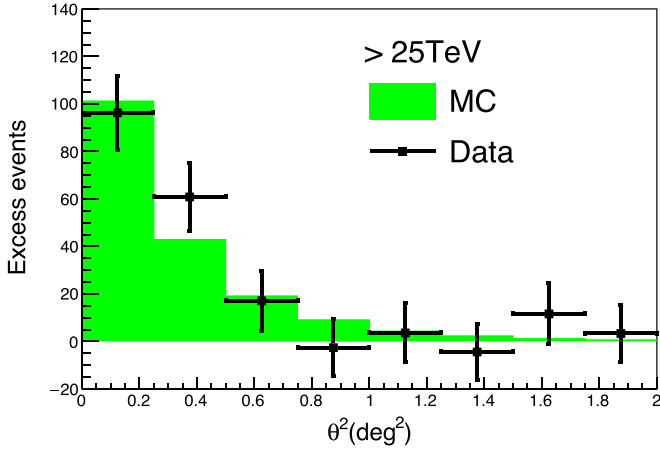


Figure 2. Distribution of events as a function of the square of the angular distance to the LHAASO J0341+5258 direction for both experimental data (black points) and MC simulation (green area). Events with energy above 25 TeV are used here.

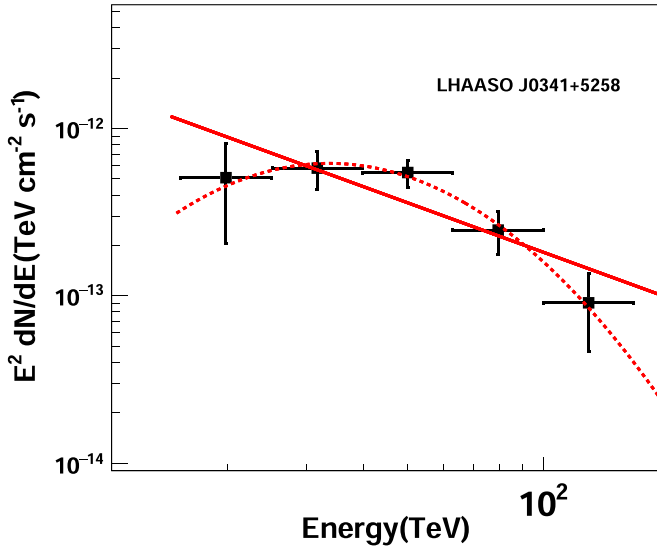


Figure 3. The energy spectrum of LHAASO J0341+5258. Only statistic errors are shown here. The solid line is the best-fit result assuming a single power-law function, and the dotted line is the result from the log-parabola function.

differential flux ($\text{TeV}^{-1}\text{cm}^{-2}\text{s}^{-1}$) in the energy range from 10 to 200 TeV is

$$\frac{dN}{dEdAdt} = (2.8 \pm 0.4_{\text{sta}} \pm 0.2_{\text{sys}}) \times 10^{-16} \left(\frac{E}{40 \text{ TeV}} \right)^{-2.98 \pm 0.19_{\text{stat}} \pm 0.02_{\text{sys}}} \quad (1)$$

The χ^2/ndf for the fit is 6.58/3. The integral flux above 25 TeV is $1.43 \times 10^{-14} \text{ (cm}^{-2}\text{s}^{-1}\text{)}$, corresponding to about 20% of the flux of the Crab Nebula. We should note that in general the atmospheric density profile always deviates from the atmosphere model used in simulations, which is the main systematic error affecting the SED. The total systematic uncertainty is estimated to be 7% for the flux and 0.02 for the spectral index. Although the power-law fit cannot be rejected, from Figure 3 one can see a noticeable steepening of an initially hard (E^{-2} type) spectrum above ≈ 50 TeV. A hard spectrum at low energies is demanded also by the flux upper limit set by Fermi-LAT around 10 GeV (see

below). Therefore, we fit the spectrum also by a log-parabola function $f(E) = J \cdot (E/E_0)^{-(\alpha + \beta \log_{10}(E/E_0))}$. The result is shown in Figure 3. The obtained best-fit parameters are $J = (3.7 \pm 0.6) \times 10^{-16} \text{ TeV}^{-1} \text{ cm}^{-2} \text{ s}^{-1}$, $\alpha = 2.4 \pm 0.4$ and $\beta = 2.6 \pm 1.3$, with $\chi^2/ndf = 0.26/2$. The improvement is about 2.5σ comparing to a single power-law fit, so we cannot get a solid conclusion now. With the accumulation of data, the behavior of the spectrum will be clearer.

4. Discussions

4.1. Multiwavelength Observations

4FGL J0340.4+5302 is the closest GeV γ -ray source in the latest Fermi-LAT source catalog (4FGL-DR2; Abdollahi et al. 2020) at an angular distance of $0^\circ.16$, which is within the extension of LHAASO J0341+5258. This source is labeled as an unidentified source in the catalog. To investigate the relationship between 4FGL J0340.4+5302 and LHAASO J0341+5258, we analyzed 12 yr of Fermi Pass 8 data (from 2008 August 4 until 2020 August 14) and performed binned likelihood analysis in the $20^\circ \times 20^\circ$ region centered on LHAASO J0341+5258 for γ -rays in the energy range of 0.1–500 GeV. We found that using the Gaussian disk model for 4FGL J0340.4+5302, the 95% C.L. upper limit of the extension (σ_{disk}) is $\leq 0^\circ.3$ while the TS value of the extension hypothesis is ~ 0.15 . By comparing the log-parabola model to a power-law model, we find its spectrum is significantly curved. The replacement of the point-source model with a Gaussian disk of $\sigma_{\text{disk}} = 0^\circ.29$ located at the center of LHAASO J0341+5258 does not influence the results. To compare with LHAASO measurement, in Figure 5 we present the SEDs and upper limits using the same spatial template of LHAASO J0341+5258.

In the X-ray domain, there are four sources in the second ROSAT all-sky survey source catalog (0.1–2.4 keV) within $0^\circ.6$ from the center of LHAASO J0341+5258. The angular distance for the four X-ray sources, named 2RXS J034125.8+525530, 2RXS J033928.5+530720, 2RXS J034316.5+524331, and 2RXS J034203.0+532329 (Boller et al. 2016), is $0^\circ.046$, $0^\circ.321$, $0^\circ.379$, and $0^\circ.434$ separately. The flux of all these 2RXS sources is not well measured, and the positions of 2RXS J033928.5+530720 and 2RXS J034316.5+524331 are coincident with 2SXPS 172133 and 2SXPS 171354 in the 2RXPS Swift X-ray telescope point-source catalog (Evans et al. 2019), respectively. The energy flux of 2SXPS 171354 and 2SXPS 172133 is $(1.6 \pm 0.7) \times 10^{-13} \text{ erg cm}^{-2} \text{ s}^{-1}$ and $(5.5 \pm 1.6) \times 10^{-13} \text{ erg cm}^{-2} \text{ s}^{-1}$ from the catalog, respectively.

We note that LHAASO J0341+5258 is indeed extended, and the flux of X-ray point sources may come from a much compact region and can have different origins. In this regard, we found that the archived Chandra ACIS observation with ID 16828 is partially overlapped with LHAASO J0341+5258. No significant emission was detected in this region. The upper limit was derived by assuming the observed X-ray flux in the overlapped region is dominated by Poisson noises. We summed over the overlapped region to get the total photon counts N and used $3\sqrt{N}$ as the 3σ upper limits of the total counts from the source. Then, we divided the counts by the exposure to derive the upper limits of the flux. Because the FoV of Chandra is significantly smaller than the derived intrinsic extension of LHAASO J0341+5258, the upper limit is then scaled by the area. Finally, the derived upper limit for LHAASO J0341+5258 is $1.5 \times 10^{-12} \text{ erg cm}^{-2} \text{ s}^{-1}$ in the energy range of 0.2–8.8 keV. It should be noted that we ignore the

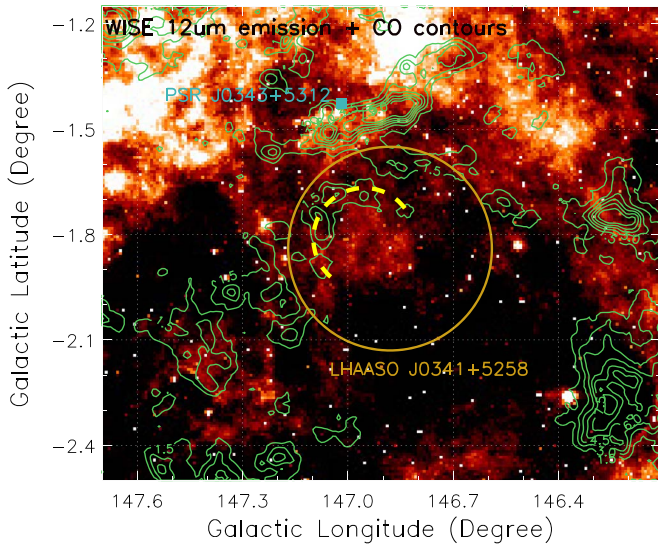


Figure 4. WISE $12\ \mu\text{m}$ emission and CO emission (green contours) toward LHAASO J0341+5258 (the golden circle). The CO emission is integrated in the velocity interval of $0\text{--}10\ \text{km s}^{-1}$ and starts from $1.5\ \text{K km s}^{-1}$ with a step of $1.5\ \text{K km s}^{-1}$. The yellow dashed line marks the half-shell CO structure. The cyan box indicates PSR J0343+5312.

absorption in the estimations, but the effects should be minor in the whole energy range, unless the column density in the line of sight is extremely large and the intrinsic X-ray flux is very soft.

HAWC detected no significant source in this region (Albert et al. 2020), but with the online interactive tools³⁵ the derived 2σ flux upper limit is $1.1 \times 10^{-12}\ \text{erg cm}^{-2}\ \text{s}^{-1}$, assuming a spectrum index of -2.5 and extension of 0.5 with a reference energy of $7\ \text{TeV}$.

The CO observations of this region from the Milky Way Imaging Scroll Painting project (Su et al. 2019) are shown in Figure 4. The molecular gas is partly overlapped with LHAASO J0341+5257, which presents a half-shell structure, labeled by the yellow dashed line. The total mass of gas within 1° of the source is about $10^3 M_\odot$ considering a distance of $1\ \text{kpc}$. Assuming the average cloud thickness of 0.5 , the H_2 cubic density is about $50\ \text{cm}^{-3}$. There is no clear CO emission at larger distances. Meanwhile, although the total CO emission is not bright in this region, the ^{13}CO line is also detected at the enhanced ^{12}CO emission region of the half-shell structure, which implies the existence of dense clumps. The critical density of ^{13}CO is about $2000\ \text{cm}^{-3}$. So the mean density of several tens of cm^{-3} is reasonable for the revealed MC in the FoV of the LHAASO source. Also in Figure 4 we can see a significant $12\ \mu\text{m}$ infrared radiation surrounded by the half-shell structure, which is inside the TeV source. One may argue that the infrared emission, molecular gas, and TeV emission are physically associated with each other, but further observations are needed to draw a firm conclusion.

4.2. Phenomenological Fitting and Possible Origin

Due to the spatial coincidence between LHAASO J0341+5258 and 4FGL J0340.4+5302, we consider at first the possibility that both sources have a unified origin. However, we note that the energy flux of Fermi-LAT observations extends to more than $1\ \text{GeV}$ and is one order of magnitude higher than that of TeV γ -rays, which makes a synchrotron origin of the

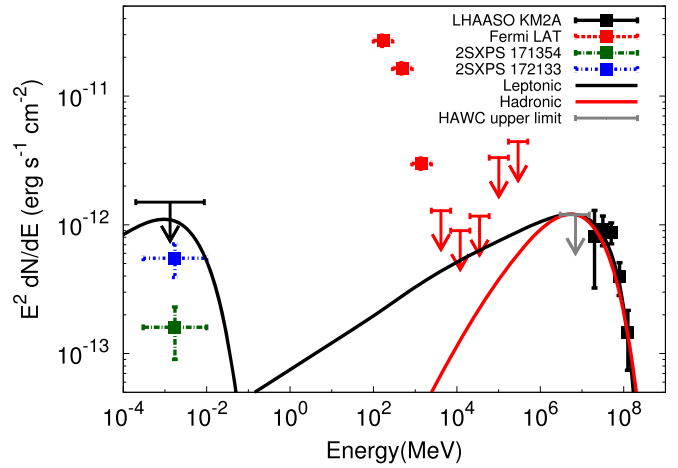


Figure 5. The multiwavelength SEDs of LHAASO J0341+5258. The black squares are the LHAASO-KM2A observations, the red points and arrows are the Fermi-LAT spectral points and upper limits, and the green and blue points are the X-ray flux for 2SXPS 171354 and 2SXPS 172133 from the 2RXPS catalog (Evans et al. 2019), respectively. The black arrow labels the upper limit derived from Chandra observations. The gray arrow is the HAWC upper limit from the online interactive tools (see the text for details). Also shown is the phenomenological fitting in both leptonic (black curves) and hadronic scenarios (red curves).

MeV–GeV emission quite unlikely. On the other hand, the spectral shape of 4FGL J0340.4+5302 reveals a sharp cutoff feature, which is quite similar to the GeV γ -ray emission of pulsars. If this is true, the TeV emission can be interpreted as originating from the inverse Compton scatterings (ICs) of the relativistic electrons in the surrounding pulsar wind nebular (PWN) or a larger structure enveloping the PWN (Aharonian 2004), the so-called pulsar halo (Sudoh et al. 2019). The observed TeV spectrum is steep, which implies that we probably observed the cutoff regions. Thus, for simplicity, we used a power-law electron spectrum with a superexponential cutoff $f(E) \sim E^{-\Gamma} \exp(-(E/E_c)^2)$. Because the KM2A data points are mainly at the cutoff region, the constraint on the index Γ is loose. We fix Γ to 2.5 to provide a schematic fit to the data. Taking into account the CMB and interstellar radiation fields (ISRFs) in the solar vicinity (Popescu et al. 2017) as the target photon fields, the fit is labeled by the black lines in Figure 5. The derived E_c is $200\ \text{TeV}$, and the total electron energy above $10\ \text{TeV}$ is about $10^{44}\ \text{erg} \left(\frac{d}{1\ \text{kpc}}\right)^2$, where d is the distance to the source. The X-ray upper limit can also be used to set the upper limit for the magnetic fields, which is $3\ \mu\text{G}$. We note that the X-ray upper limit was derived from a much smaller region than the VHE emission region; a dedicated study with the instruments with larger FoV is required to get more robust constraints. The upper limit of $3\ \mu\text{G}$ is feasible for both the PWN or pulsar halo case. Due to the unknown distance and thus the unknown physical size of this source, it is hard to distinguish the PWN or pulsar halo scenarios. The search for the pulsation of the GeV data of 4FGL 0340.4+5302 would be useful to test such a scenario, and Version 1.21 of the ATNF (Australia Telescope National Facility) Pulsar Catalogue lists another pulsar within an angular distance of 0.4° away from LHAASO J0341+5258 (Damashek et al. 1978). PSR J0343+5312 has a distance of $2.48\ \text{kpc}$, age of $2.28\ \text{Myr}$, and spin-down luminosity of $7.3 \times 10^{31}\ \text{erg s}^{-1}$,

³⁵ <https://data.hawc-observatory.org/datasets/3hwc-survey/coordinate.php>

which seems too weak and too old to account for the VHE γ -ray emissions, even in the pulsar halo scenario.

Finally, although there are no known hadronic accelerators such as SNRs in this region, we cannot formally rule out the hadronic origin. Indeed, as mentioned in the last section, there are hints that the TeV emissions are correlated with infrared emission as well as a weak CO shell structure. The ambient gas density of 50 cm^{-3} is used in the phenomenological hadronic fittings. To fit the LHAASO-KM2A data points, we found that for parent protons with spectral index larger than 2, the predicted γ -ray spectrum will violate the upper limit at 10 GeV derived from Fermi-LAT data (see Figure 5). We present a schematic fit to the γ -ray data by fixing the index to 1.5 and with the best-fit proton spectrum of $f(E) \sim E^{-1.5} \exp(-E/190 \text{ TeV})$, which is labeled by the red curve in Figure 5. Note that this spectrum is too hard compared to the cosmic-ray spectrum predicted by the diffusive shock acceleration applied to young SNRs. On the other hand, it can be naturally explained by cosmic rays that have escaped the SNR and hit a cloud located within a proximity of $\sim 100 \text{ pc}$ of a middle-aged or older (previously invisible) SNR (Gabici & Aharonian 2007). The derived total energy in protons above 10 TeV is $1.5 \times 10^{46} \left(\frac{d}{1 \text{ kpc}}\right)^2 \left(\frac{50 \text{ cm}^{-3}}{n}\right) \text{ erg}$, where n is the ambient gas density.

5. Conclusions

Since 2019 December, half of the LHAASO-KM2A experiment has monitored the sky in the decl. band from -15° to 75° above tens of TeV with a high duty cycle. An excess with a pretrial significance of 8.2σ was detected from the direction of LHAASO J0341+5258 using events with energy above 25 TeV. LHAASO J0341+5258 is an extended source with a width of $\sigma = (0.29 \pm 0.06_{\text{stat}} \pm 0.02_{\text{sys}})^\circ$. The energy spectrum can be approximately described by a power law, even though there is a hint of a curvature at around 50 TeV. The integrated energy flux of γ -ray emissions above 25 TeV is $1.44 \times 10^{-14} \text{ (cm}^{-2} \text{ s}^{-1})$, which accounts for about 20% of the flux from the Crab Nebula.

The source is positionally coincident with the GeV γ -ray source 4FGL J0340.4+5302 observed by Fermi-LAT (Abdollahi et al. 2020). The upper limit of the latter at 10 GeV demands a hard spectrum of LHAASO J0341+5258 (photon index < 2) when extrapolating toward low energies. Together with the fast drop of the γ -ray fluxes above 50 TeV, in the phenomenological fitting in the leptonic and hadronic scenarios, the power-law requires the indices of the parent electrons and protons to be 2.5 and 1.5, with cutoffs of about 200 TeV and 190 TeV, respectively. The most likely realization of the leptonic scenario is the extended emission of a PWN and/or a pulsar halo. The challenge for this scenario is the lack of a reported powerful pulsar. Interestingly, such a pulsar could be the gamma-ray source 4FGL J0340.4+5302 with a characteristic spectrum below 1 GeV. The detection of pulsed radio emission from this source would support the IC origin of the UHE gamma-ray emission. The hadronic origin of the UHE emission can be interpreted as an ‘‘echo’’ from a molecular cloud(s)—the result of interactions of protons with dense gas regions in the proximity of an old (currently invisible) SNR.

This work is supported in China by the National Key R&D program of China under grants 2018YFA0404201, 2018YFA0404202, 2018YFA0404203, and 2018YFA0404204; by NSFC (No. 12022502, No. 11905227, No. 11635011, and No. U1931112); and in Thailand by RTA6280002 from Thailand Science Research and Innovation. The authors would like to thank

all staff members who work at the LHAASO site above 4400 m above sea level year-round to maintain the detector and keep the electrical power supply and other components of the experiment operating smoothly. We are grateful to the Chengdu Management Committee of Tianfu New Area for their constant financial support of research with LHAASO data.

This research made use of the data from the Milky Way Imaging Scroll Painting (MWISP) project, which is a multiline survey in $^{12}\text{CO}/^{13}\text{CO}/^{18}\text{CO}$ along the northern galactic plane with the PMO-13.7 m telescope. We are grateful to all the members of the MWISP working group, particularly the staff members at the PMO-13.7 m telescope, for their long-term support. MWISP was sponsored by the National Key R&D Program of China with grant 2017YFA0402701 and the CAS Key Research Program of Frontier Sciences with grant QYZDJ-SSW-SLH047.




Appendix Fermi-LAT Analysis

Because LHAASO J0341+5258 is extended, we first use fermipy (Wood et al. 2017) to reinvestigate the location and extension of 4FGL J0340.4+5302 using events with energy range of 1–500 GeV and the Gaussian disk model. We found that the best-fit positions of both localization and extension test are basically consistent with the original location of 4FGL J0340.4+5302 in the 4FGL catalog. Moreover, the TS value of the extension is only ~ 0.15 , and the 95% C.L. upper limit of the extension (σ_{disk}) is ≤ 0.3 , which is consistent with the results of the KM2A observation. However, its central position is about $0^\circ 15'$ away from LHAASO J0341+5258. To test whether the spectrum of 4FGL J0340.4+5302 is curved, we compared a simple power-law model to a log-parabola model, i.e., $dN/dE = N_0 (E/E_b)^{-\alpha - \beta \log(E/E_b)}$. The likelihood of the log-parabola model $\mathcal{L}_{\text{LogP}}$ is increased by ~ 125 compared to that of the power-law model $\mathcal{L}_{\text{LogP}}$. Thus $TS_{\text{curve}} \equiv 2 \log(\mathcal{L}_{\text{LogP}}/\mathcal{L}_{\text{PL}}) = 250$, which means that the spectrum of 4FGL J0340.4+5302 is significantly curved. For 4FGL J0340.4+5302, the best-fit spectral parameter of its log-parabola model $\alpha = 3.15 \pm 0.05$ and $\beta = 0.51 \pm 0.05$, and the energy flux is $\sim 5.0 \times 10^{-11} \text{ erg cm}^{-2} \text{ s}^{-1}$ in the energy range of 0.1–500 GeV, corresponding to a significance of $\sim 56\sigma$ ($TS \simeq 3149$).

Next, we replaced the spatial model of 4FGL J0340.4+5302 with a Gaussian disk of $\sigma_{\text{disk}} = 0^\circ 29'$ located at the center of LHAASO J0341+5258, as a representative of LHAASO J0341+5258 at the GeV band. Through the likelihood analysis, we found that the spectral shape and total flux of this GeV LHAASO source are very similar to those of 4FGL J0340.4+5302 as we obtained above, but such replacement does not increase the total likelihood compared to the original Fermi 4FGL-DR2 source model.

Then, we divided the energy range 0.1–500 GeV into eight logarithmically spaced energy bins and derived the SEDs using the 4FGL catalog point-like source J0340.4+5302 and the GeV representative of LHAASO J0341+5258, respectively. We found in both cases that the overall spectra are very soft, and no significant emissions above 2 GeV are detected, and thus only upper limits are derived for their flux above 2 GeV.

ORCID iDs

F. Aharonian  <https://orcid.org/0000-0003-1157-3915>
S. Z. Chen  <https://orcid.org/0000-0003-0703-1275>
Cong Li  <https://orcid.org/0000-0002-2617-2455>

References

- Abdollahi, S., Acero, F., Ackermann, M., et al. 2020, *ApJS*, **247**, 33
- Abeysekara, A. U., Albert, A., Alfaro, R., et al. 2020, *PhRvL*, **124**, 021102
- Aharonian, F., An, Q., Axikegu, et al. 2021, *ChPhC*, **45**, 025002
- Aharonian, F., Yang, R., & de Oña Wilhelmi, E. 2019, *NatAs*, **3**, 561
- Aharonian, F. A. 2004, *Very High Energy Cosmic Gamma Radiation: A Crucial Window on the Extreme Universe* (Singapore: World Scientific Publishing Co. Pte. Ltd.)
- Aharonian, F. A. 2013, *APh*, **43**, 71
- Albert, A., Alfaro, R., Alvarez, C., et al. 2020, *ApJ*, **905**, 76
- Amenomori, M., Bao, Y. W., Bi, X. J., et al. 2019, *PhRvL*, **123**, 051101
- Bednarek, W., & Protheroe, R. J. 2002, *APh*, **16**, 397
- Boller, T., Freyberg, M. J., Trümper, J., et al. 2016, *A&A*, **588**, A103
- Cao, Z., Aharonian, F. A., An, Q., et al. 2021, *Natur*, **594**, 33
- Cao, Z., Chen, M.-J., Song-Zhan Hu, H.-B., et al. 2019, *ChA&A*, **43**, 457
- Damashek, M., Taylor, J. H., & Hulse, R. A. 1978, *ApJL*, **225**, L31
- Evans, P. A., Page, K. L., Osborne, J. P., et al. 2019, *yCat*, IX, 58
- Fleysher, R., Fleysher, L., Nemethy, P., Mincer, A. I., & Haines, T. J. 2004, *ApJ*, **603**, 355
- Gabici, S., & Aharonian, F. A. 2007, *ApJL*, **665**, L131
- He, H. 2018, *Radiation Detection Technology and Methods*, **2**, 7
- HESS Collaboration, Abramowski, A., & Aharonian, F. 2016, *Natur*, **531**, 476
- Lv, H., He, H., Sheng, X., et al. 2018, *APh*, **100**, 22
- Popescu, C. C., Yang, R., Tuffs, R. J., et al. 2017, *MNRAS*, **470**, 2539
- Su, Y., Yang, J., Zhang, S., et al. 2019, *ApJS*, **240**, 9
- Sudoh, T., Linden, T., & Beacom, J. F. 2019, *PhRvD*, **100**, 043016
- Wilks, S. S. 1938, *Ann. Math. Statist*, **9**, 60
- Wood, M., Caputo, R., Charles, E., et al. 2017, *Proc. ICRC (Busan)*, **35**, 824